Flow-induced transitions of red blood cell shapes under shear

Johannes Mauer[1,*], Simon Mendez[2,*], Luca Lanotte[3], Franck Nicoud[2], Manouk Abkarian[3], Gerhard Gompper[1], and Dmitry A. Fedosov[1,†]
[1] *Institute of Complex Systems and Institute for Advanced Simulation, Forschungszentrum Jülich, 52425 Jülich, Germany*
[2] *IMAG, University of Montpellier, CNRS, 34095 Montpellier, France*
[3] *Centre de Biochimie Structurale, CNRS UMR 5048 - INSERM UMR 1054, University of Montpellier, 34090 Montpellier, France*

A recent study of red blood cells (RBCs) in shear flow [Lanotte et al., Proc. Natl. Acad. Sci. USA 113, 13289 (2016)] has demonstrated that RBCs first tumble, then roll, transit to a rolling and tumbling stomatocyte, and finally attain polylobed shapes with increasing shear rate, when the viscosity contrast between cytosol and blood plasma is large enough. Using two different simulation techniques, we construct a state diagram of RBC shapes and dynamics in shear flow as a function of shear rate and viscosity contrast, which is also supported by microfluidic experiments. Furthermore, we illustrate the importance of RBC shear elasticity for its dynamics in flow and show that two different kinds of membrane buckling trigger the transition between subsequent RBC states.

The behavior of red blood cells (RBCs) in flow have been a fascinating research topic for several decades, due to the direct biological relevance and intriguing physical mechanisms which govern the observed cell shapes and dynamics. First observations of RBCs in linear shear flow have shown that RBCs tumble (TB) or flip as a coin at low shear stresses and tank-tread (TT) at high enough shear stresses [1–4]. A TT-RBC adopts a nearly stationary orientation in shear flow and its membrane performs rotating motion [1, 3, 4]. The transition between the two motions is due to the existence of a minimum of elastic energy when the membrane is in static equilibrium, which is referred to as shape memory [5] and has been incorporated into the theoretical models for RBC dynamics [6, 7]. Recently, another dynamics, RBC rolling, which appears at moderate shear stresses in-between those resulting in cell TB and TT, has been discussed [8–10]. Rigid-like TB motion at low shear stresses is destabilized by a possible movement of the elastic cytoskeleton of a RBC [10] and the cell shows first a TB motion with a precession in its orientation axis, followed by the rolling motion for increasing shear stresses [10–12]. A similar behavior has been also found for oblate capsules [13, 14].

Most of the mentioned studies have been performed under conditions with a low viscosity ratio $\lambda < 1$ between intracellular and extracellular fluids. This means that RBCs are suspended into highly viscous fluids in comparison to blood plasma, as $\lambda \approx 5$ under physiological conditions. The use of a high-viscosity fluid medium has been driven by the limitations of experimental devices and cell-tracking at high shear rates, because the high viscosity allows the application of high shear stresses at moderate shear rates. However, the viscosity ratio λ has been shown to play a crucial role in vesicle [15–17] dynamics in shear flow, such that an increase in λ induces the transition from vesicle TT at low λ to TB at high λ [15, 18]. Recent simulations of RBCs in shear flow have also reported TB at large enough λ values [19]. Other numerical investigations of RBCs [20] and oblate capsules [14] in shear flow have reported a stable rolling motion for large enough viscosity contrasts and shear rates. In contrast, a recent study [21] on blood rheology has found that RBCs at $\lambda \approx 5$ first tumble, then roll, deform into rolling stomatocytes, and finally adopt highly-deformed polylobed shapes as the shear rate is gradually increased. Polylobed shapes have also been reported in early experiments on RBCs [22] and in a theoretical study on elastic capsules [23].

In this Letter, we take a closer look at these dynamic shapes and transitions between them. In contrast, Ref. [21] was focused on the effect of these shapes on blood rheology. We construct a state diagram, which presents the observed shapes and dynamics of RBCs for a wide range of shear rates and viscosity contrasts. Then, we focus on RBC dynamics at $\lambda > 1$ and show that two of the most salient shape transitions are controlled by membrane buckling due to cell compression. These results highlight the essential role of the elastic cytoskeleton for RBC motion under physiological flow conditions.

Shapes and dynamics of RBCs are obtained from three-dimensional simulations using two different hydrodynamic techniques. The first method corresponds to a mesoscopic particle-based approach, smoothed dissipative particle dynamics (SDPD) [24, 25], for modeling fluid flow, while a RBC membrane is represented by a triangulated network of springs [26–28] whose vertices are coupled to the fluid via frictional forces. The network assumes fixed connectivity and includes the spring's elastic energy, bending energy, and area- and volume-conservation constraints [27, 29]. The second simulation method relies on a finite-volume parallel solver for the incompressible Navier-Stokes equations on unstructured meshes, YALES2BIO [30, 31]. Fluid-structure coupling is implemented using an immersed boundary method adapted to unstructured grids [30]. RBCs are discretized by a moving Lagrangian mesh and modeled as viscous

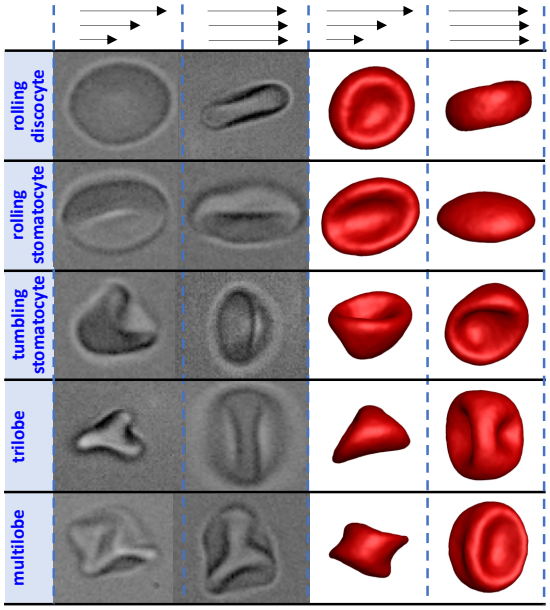

FIG. 1. RBC shapes observed in microfluidic experiments ($\lambda \approx 8$) and SDPD simulations ($\lambda \approx 5$) at various dimensionless shear rates $\dot{\gamma}^* = \dot{\gamma}\tau$ ($\tau \approx 1.2 \times 10^{-3}$ s). The shapes are rolling discocyte, rolling stomatocyte, TB stomatocyte, trilobe, and multilobe, observed at $\dot{\gamma}^* = 0.014$, 0.2, 0.34, 1, and 2.5 in experiments and at $\dot{\gamma}^* = 0.014$, 0.18, 0.34, 0.93, and 3.3 in simulations, respectively. Two views, vorticity and flow-gradient directions, are shown by the arrows with unequal and equal lengths, respectively. See also movies S1-S4.

drops enclosed by membranes resisting shear, bending, and area dilation [31]. More details on the methods can be found in supplemental material. Simulations are complemented by experiments of a pressure-driven flow within a 50 μm-diameter capillary. RBCs are suspended in a PBS/BSA solution with a viscosity of $\eta = 9 \times 10^{-4}$ Pa·s at a volume fraction of 1% at 25^o C. Local shear rates are estimated by measuring both the local cell velocity and distance from the capillary walls. Only RBCs flowing at a distance in the range between 10 and 20 μm from the channel wall are considered.

To non-dimensionalize the shear rate $\dot{\gamma}$, a characteristic RBC time $\tau = \eta D/\mu$ is defined, where $D = \sqrt{A/\pi}$ is an effective RBC diameter and A is the surface area, μ is the membrane shear modulus, and η is the dynamic viscosity of a suspending medium. Average properties of healthy RBCs are taken to be $A = 134 \times 10^{-12}$ m^2 [32] (i.e., $D = 6.5 \times 10^{-6}$ m) and $\mu = 4.8 \times 10^{-6}$ N/m. Thus, with $\eta = 9 \times 10^{-4}$ Pa·s the characteristic time is $\tau \approx 1.2 \times 10^{-3}$ s. Membrane bending rigidity is set to $\kappa = 70 k_B T = 3 \times 10^{-19}$ J (k_B is the Boltzmann constant and T is temperature) such that the Föppl-von Kármán number $\alpha = \mu D^2/\kappa = 680$ is fixed in all cases. The stress-free shape of a RBC elastic network is assumed to be an oblate spheroid with a reduced volume of 0.96. The stress-free shape of a RBC membrane affects the TB-to-TT transition [12, 20, 33], such that a nearly spherical stress-free shape leads to shear rates of the transition consistent with experiments [6, 10], while a biconcave stress-free shape shifts the TB-to-TT transition to larger shear rates [12, 20, 33].

Figure 1 illustrates observed shapes in microfluidic experiments ($\lambda \approx 8$) and SDPD simulations ($\lambda \approx 5$). Different shapes, including rolling discocyte and stomatocyte, TB stomatocyte, trilobe, and multilobe, are shown from two views, vorticity and flow-gradient directions (see also movies S1-S4). By collecting a number of simulations for different dimensionless shear rates $\dot{\gamma}^* = \dot{\gamma}\tau$ (or Capillary numbers) and viscosity contrasts λ, we construct the RBC shape diagram shown in Fig. 2. At very low shear rates ($\dot{\gamma}^* \lesssim 7 \times 10^{-3}$), RBCs tumble (not shown). With increasing shear rate, the cells first transit to a rolling discocyte and then to a rolling stomatocyte. At high shear rates, λ plays an important role, and TT occurs for $\lambda \lesssim 3.2$, while RBCs exhibit multilobe shapes for $\lambda \gtrsim 3.2$. Interestingly, the transitions between different states for $\lambda \gtrsim 3.2$ are governed predominantly by $\dot{\gamma}^*$ and are nearly independent of λ. Note that the transitions between different shapes and dynamics are very similar from the two numerical methods.

Figure 2 also contains ~~a few~~ experimental points to support the simulation-based diagram. For example, the transition to TT for $\lambda \lesssim 1$ occurs at $\dot{\gamma}^* \approx 0.11$, corresponding to a critical shear stress of $\eta\dot{\gamma} \approx 0.08$ Pa, which is consistent with values in Refs. [6, 10]. In contrast to the simulations, where a single RBC state is found for fixed flow conditions, our microfluidic experiments do not show a single RBC shape or dynamics for a fixed shear stress, but yield a distribution of different states, see Figs. S1 and S2. Therefore, the diamond symbols in Fig. 2 represent most probable states for a fixed shear stress and are intended for a qualitative comparison with simulations. The main reason for a non-unique shape or dynamics observed in experiments is likely a strong ~~enough~~ variability in RBC membrane properties (e.g. shear elasticity, bending rigidity, cytosol viscosity), which does not permit an exact determination of $\dot{\gamma}^*$ and λ. All experimental shear rates are normalized with $\tau \approx 1.2 \times 10^{-3}$ s.

To look in more detail into the transitions between different states, we have computed RBC total energy, as shown in Fig. 3(a) for a RBC with $\lambda = 5$ from YALES2BIO simulations. As expected, the RBC total energy is a monotonically increasing function of shear rate, because the cell gets more and more deformed by the shear forces. However, we observe effective power laws with decreasing exponents as we go from one dynamic state to the other, as shown by the lines in Fig. 3(a). This implies that RBCs adopt an energetically more favorable dynamics, even though no energy minimum principles can be invoked here. Therefore, there are no simple energy arguments which could explain the existence of the shapes and transitions at specific $\dot{\gamma}^*$.

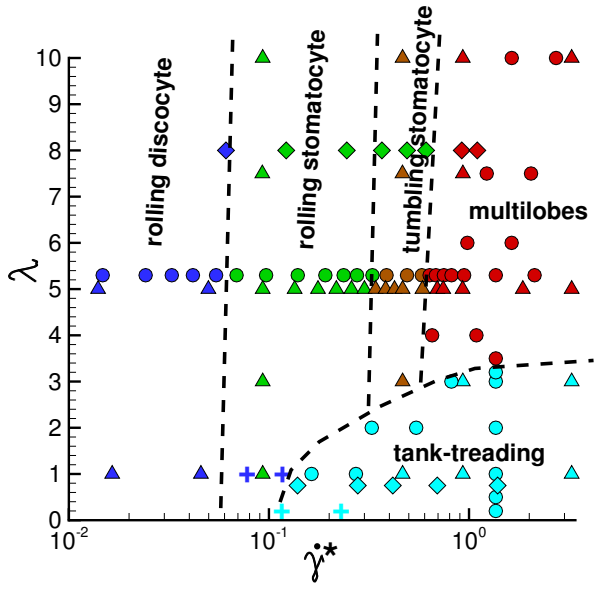

FIG. 2. Shapes and dynamics of RBCs in shear flow as a function of $\dot{\gamma}^*$ and λ. Different areas, representing rolling discocyte, rolling stomatocyte, TB stomatocyte, TT, and multilobes, are based on simulation results, where dashed lines serve as a guide to the eyes. Two sets of simulations are denoted by triangles (SDPD) and circles (YALES2BIO). The colors indicate RBC shape or dynamics. All simulation data are for Föppl-von Kármán number $\alpha = \mu D^2/\kappa = 680$. The set of circles at $\lambda \approx 5.3$ corresponds to simulations at $\lambda = 5$ and is just shifted up in the diagram for visual clarity. The plus symbols correspond to experiments from Ref. [10]. Diamond symbols represent most probable states from our microfluidic experiments, since no unique state, but a distribution of different states is obtained for fixed flow conditions, see distributions in Figs. S1 and S2. The experimental shear rates are normalized by $\tau \approx 1.2 \times 10^{-3}$ s.

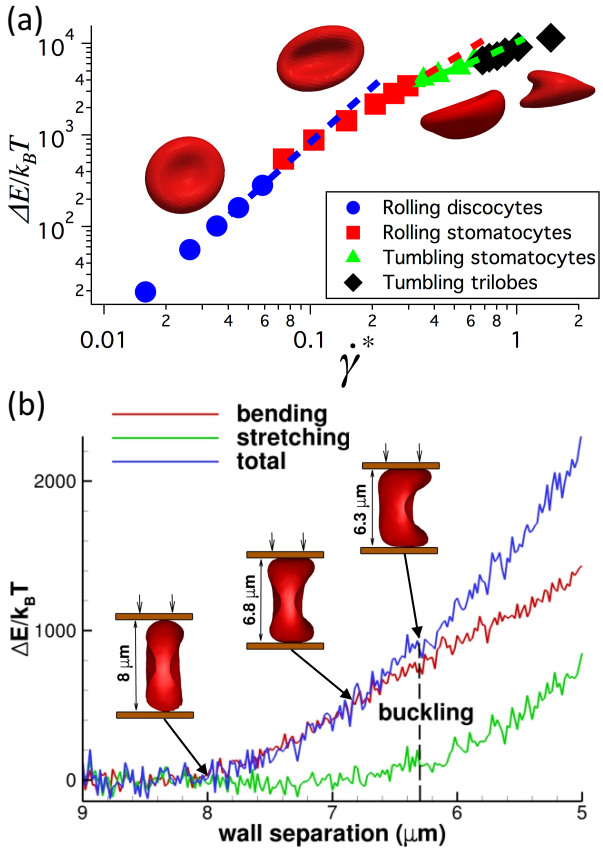

FIG. 3. Transition between different shapes and dynamics at $\lambda = 5$. (a) Change in RBC total energy, including shear and bending elasticity, from YALES2BIO simulations as a function of shear rate. (b) Change in shear-elasticity and bending energies of a RBC compressed between two plates in SDPD simulations. The cell buckles from a discocyte to a stomatocyte shape, when the distance between plates becomes approximately 6.3 μm (see movie S5).

To identify transition mechanisms between different shapes and dynamics, we monitor RBC behavior for increasing $\dot{\gamma}^*$. First, a TB-RBC in shear flow transits to a rolling discocyte at low shear rates. Here, a precession in the TB axis (i.e. the TB axis does not remain within the shear plane) is first observed, followed by a complete alignment of the RBC axis with the vorticity direction as the shear rate is increased [10–12]. This transition has been described for $\lambda < 1$ [10], and therefore, it is expected to have the same origin for λ larger than unity.

As the shear rate is further increased at $\lambda = 5$, a rolling discocyte transits to a rolling stomatocyte. This transition might occur due to membrane buckling, but it is difficult to observe and confirm this effect directly in shear flow. Therefore, we consider two types of cell deformation (stretching and compression), which occur in shear flow. To mimic the elongational component of the flow, a RBC is stretched (without flow) [27, 31] similar to the RBC deformation by optical tweezers [34, 35]. Even for very strong stretching deformations, a RBC maintains both of its dimples and no transition to a stomatocyte-like shape occurs. Second, we place a RBC with its largest diameter of about 8 μm between two parallel walls, as shown in the insets of Fig. 3(b), and compress the cell by moving the upper wall down. When the distance between the walls becomes approximately 6.3 μm, the RBC exhibits buckling and a biconcave shape with dimples on both sides transits to a stomatocyte (see movie S5). Figure 3(b) presents the evolution of shear-elastic and bending energies, and near the buckling transition a small step in the elastic energy can be recognized. Note that the RBC buckling under compressive deformation occurs for the model with a nearly spherical stress-free shape (reduced volume of 0.96), while for a biconcave stress-free shape (reduced volume of 0.64), a RBC does not transit to a stomatocyte under direct compression. Simulations of a RBC with the biconcave stress-free shape at $\lambda = 5$ in shear flow show no transition from the rolling discocyte to the rolling stomatocyte, in agreement with the

compression simulation. Furthermore, a RBC with the biconcave stress-free shape transits from the rolling discocyte to a tumbling stomatocyte at $\dot{\gamma}^* \approx 0.4$ and then to a trilobe at $\dot{\gamma}^* \approx 0.72$; these values are slightly larger than the corresponding transitions for a RBC with the near spherical stress-free shape, occurring at $\dot{\gamma}^* \approx 0.32$ and $\dot{\gamma}^* \approx 0.65$, respectively. This implies that the stress-free shape of spectrin network of a RBC is likely to be close to a sphere, consistent with previous studies [12, 20]. The transition from rolling discocyte to rolling stomatocyte for a RBC with the nearly spherical stress-free shape occurs for all considered viscosity contrasts in Fig. 2, and therefore, it should be also present at low λ. However, we observe a slight shift of this transition to higher shear rates with increasing λ, since cell compression by shear flow at a fixed shear rate is reduced.

Following the rolling-stomatocyte state at $\lambda = 5$, a transition to a TB stomatocyte and then to multilobe shapes is observed for increasing $\dot{\gamma}^*$. Hence, cell rolling becomes unstable when its deformation in shear flow becomes strong enough. Similarly, in the compression test described above (Fig. 3(b)), a stomatocytic shape becomes unstable at a certain compression when confinement between the planes is further increased (not shown).

The transition to multilobe shapes can be also achieved from TT by increasing λ at high shear rates ($\dot{\gamma}^* \gtrsim 0.6$). Figure 4(a) shows the inclination angle and the aspect ratio of a TT-RBC as a function of viscosity contrast at $\dot{\gamma}^* = 1.36$. As λ increases, both the cell's extension and the inclination angle reduce. Approximately at $\lambda \approx 3.2$, a transition to multilobe shapes occurs, even though the inclination angle is still non-zero and equal to about 5°. Figure 4(b) illustrates the time evolution of RBC shapes at this transition; the membrane first forms small bumps at the top and the bottom, then very rapidly forms more lobes, and finally attains a trilobe shape (see movie S6). This is another example of a buckling transition mediated by the elasticity of the membrane, as shown in Fig. 4(c), which displays membrane's elastic tension at four time instances with the corresponding shapes in Fig. 4(b). In particular, Fig. 4(c) demonstrates that large parts of the membrane experience negative tension in both principal directions, which is most pronounced in regions of membrane buckling. A similar appearance of local negative tension has been also reported for elastic capsules in shear flow [37]. A comparison of the inclination angle for RBCs to the Keller-Skalak (KS) theory for fluid vesicles [36] in Fig. 4(a) shows a good agreement for $\lambda \lesssim 0.5$, but strong discrepancies for $\lambda \gtrsim 0.5$. Hence, the KS theory fails to predict the TT-to-trilobe transition with increasing λ for RBCs, due to both the non-ellipsoidal shape of RBCs and the strong compressions of the membrane, which lead to membrane buckling and negative inclination.

Recent simulations [19, 20] of RBCs at $\lambda \gtrsim 5$ in shear flow have reported TB at high shear rates, which is clearly different from the multilobe dynamics we observe in our experiments and simulations. A potential explanation for this discrepancy is that the simulations in Refs. [19, 20] are rather short ($\dot{\gamma}t \approx 100$), while our simulations indicate that $\dot{\gamma}t \gtrsim 200$ is often required to observe stable multilobe shapes.

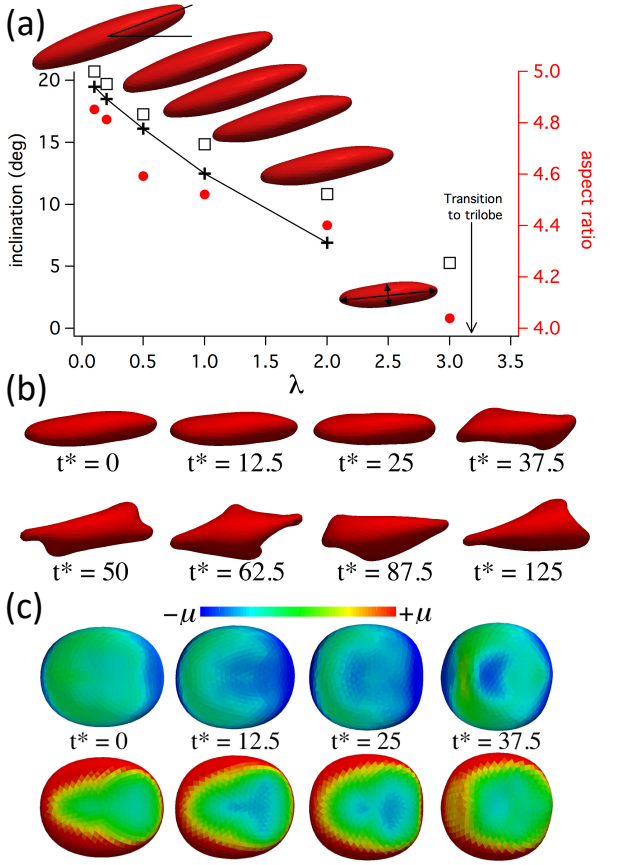

FIG. 4. Trilobe formation. (a) Inclination angle (square and plus symbols, left axis) and aspect ratio (maximum to minimum size, red bullets, right axis) of a RBC as a function of λ at $\dot{\gamma}^* = 1.36$ from YALES2BIO simulations. The square and bullet symbols correspond to simulation measurements, while the plus symbols are obtained from the Keller-Skalak theory for fluid vesicles [36] using cell dimensions measured in simulations. (b) Time evolution ($t^* = \dot{\gamma}t$) of shapes at $\lambda = 3.5$ (starting from a simulation with $\lambda = 3.1$), when TT becomes unstable and a trilobe is formed (see movie S6). (c) Membrane's elastic tension in the direction of the smallest (top) and largest (bottom) local strains.

A good qualitative agreement between simulations and experiments suggests that the viscosity of a RBC membrane likely has a secondary effect on the RBC shape diagram in Fig. 2, since it was not considered in the simulations. For instance, membrane viscosity is known to affect the TT frequency of RBC membrane [27, 38], where a shearing motion of the membrane occurs. A plausible explanation for a secondary role of membrane viscosity here is that most observed shapes (except TT) do no exhibit a significant in-plane shearing of the membrane,

such that a RBC mainly performs rotational motion (i.e. TB, rolling, rotating trilobe) in shear flow.

In summary, a diagram of RBC shapes and dynamics is presented for a wide range of shear rates and viscosity ratios. In particular, physiological conditions of $\lambda \approx 5$ are thoroughly investigated. Furthermore, we show that membrane buckling due to RBC compression in flow drives the transition between rolling discocytes and stomatocytes and determines the appearance of multilobar shapes at large λ and $\dot{\gamma}^*$. Interestingly, membrane buckling occurs ~~at~~ lower shear stresses for a RBC with the nearly spherical stress-free shape than for a RBC with the biconcave stress-free shape. The buckling mechanism for the shape transitions highlights the importance of RBC shear elasticity and stress-free shape for its dynamics in flow.

This work was supported by the Banque Publique d'Investissement project Dat@Diag, Labex Numev Convention grant ANR-10-LABX-20 (Rheoblood project). D.A.F. acknowledges funding by the Alexander von Humboldt Foundation. SDPD simulations were performed at the Jülich Supercomputing Center. YALES2BIO simulations have used HPC resources from HPC@LR and GENCI-CINES (grants 2016-c2016037194 and 2017-A0020307194).

* J.M. and S.M. contributed equally to this work.

† Corresponding author: d.fedosov@fz-juelich.de

[1] H. Schmid-Schönbein and R. Wells, Science **165**, 288 (1969).
[2] H. L. Goldsmith and J. Marlow, Proc. R. Soc. Lond. B **182**, 351 (1972).
[3] T. M. Fischer, M. Stöhr-Liesen, and H. Schmid-Schönbein, Science **202**, 894 (1978).
[4] R. Tran-Son-Tay, S. P. Sutera, and P. R. Rao, Biophys. J. **46**, 65 (1984).
[5] T. M. Fischer, Biophys. J. **86**, 3304 (2004).
[6] M. Abkarian, M. Faivre, and A. Viallat, Phys. Rev. Lett. **98**, 188302 (2007).
[7] J. M. Skotheim and T. W. Secomb, Phys. Rev. Lett. **98**, 078301 (2007).
[8] M. Bitbol, Biophys. J. **49**, 1055 (1986).
[9] W. Yao, Z. Wen, Z. Yan, D. Sun, W. Ka, L. Xie, and S. Chien, J. Biomech. **34**, 1501 (2001).
[10] J. Dupire, M. Socol, and A. Viallat, Proc. Natl. Acad. Sci. USA **109**, 20808 (2012).
[11] D. Cordasco and P. Bagchi, Phys. Fluids **25**, 091902 (2013).
[12] Z. Peng, A. Mashayekh, and Q. Zhu, J. Fluid Mech. **742**, 96 (2014).
[13] T. Omori, Y. Imai, T. Yamaguchi, and T. Ishikawa, Phys. Rev. Lett. **108**, 138102 (2012).
[14] C. Dupont, F. Delahaye, D. Barthes-Biesel, and A.-V. Salsac, J. Fluid Mech. **791**, 738 (2016).
[15] M.-A. Mader, V. Vitkova, M. Abkarian, A. Viallat, and T. Podgorski, Eur. Phys. J. E **19**, 389 (2006).
[16] V. Vitkova, M.-A. Mader, B. Polack, C. Misbah, and T. Podgorski, Biophys. J. **95**, L33 (2008).
[17] A. Farutin and C. Misbah, Phys. Rev. Lett. **109**, 248106 (2012).
[18] V. Kantsler and V. Steinberg, Phys. Rev. Lett. **96**, 036001 (2006).
[19] K. Sinha and M. D. Graham, Phys. Rev. E **92**, 042710 (2015).
[20] D. Cordasco, A. Yazdani, and P. Bagchi, Phys. Fluids **26**, 041902 (2014).
[21] L. Lanotte, J. Mauer, S. Mendez, D. A. Fedosov, J.-M. Fromental, V. Claveria, F. Nicoud, G. Gompper, and M. Abkarian, Proc. Natl. Acad. Sci. USA **113**, 13289 (2016).
[22] T. Fischer and H. Schmid-Schönbein, Blood Cells **3**, 351 (1977).
[23] A. Helmy and D. Barthés-Biesel, J. Mec. Theor. Appl. **1**, 859 (1982).
[24] P. Español and M. Revenga, Phys. Rev. E **67**, 026705 (2003).
[25] K. Müller, D. A. Fedosov, and G. Gompper, J. Comp. Phys. **281**, 301 (2015).
[26] H. Noguchi and G. Gompper, Proc. Natl. Acad. Sci. USA **102**, 14159 (2005).
[27] D. A. Fedosov, B. Caswell, and G. E. Karniadakis, Biophys. J. **98**, 2215 (2010).
[28] D. A. Fedosov, H. Noguchi, and G. Gompper, Biomech. Model. Mechanobiol. **13**, 239 (2014).
[29] D. A. Fedosov, M. Peltomäki, and G. Gompper, Soft Matter **10**, 4258 (2014).
[30] S. Mendez, E. Gibaud, and F. Nicoud, J. Comp. Phys. **256**, 465 (2014).
[31] J. Sigüenza, S. Mendez, and F. Nicoud, Biomech. Model. Mechanobiol. **16**, 1645 (2017).
[32] E. A. Evans and R. Skalak, *Mechanics and thermodynamics of biomembranes* (CRC Press, Inc., Boca Raton, Florida, 1980).
[33] J. Dupire, M. Abkarian, and A. Viallat, Soft Matter **11**, 8372 (2015).
[34] S. Henon, G. Lenormand, A. Richert, and F. Gallet, Biophys. J. **76**, 1145 (1999).
[35] M. Dao, C. T. Lim, and S. Suresh, J. Mech. Phys. Solids **51**, 2259 (2003).
[36] S. R. Keller and R. Skalak, J. Fluid Mech. **120**, 27 (1982).
[37] E. Foessel, J. Walter, A.-V. Salsac, and D. Barthes-Biesel, J. Fluid Mech. **672**, 477 (2011).
[38] A. Yazdani and P. Bagchi, J. Fluid Mech. **718**, 569 (2013).